

Computer-Aided Design and Analysis of Spectrally Aligned Hybrid Plasmonic Nanojunctions for SERS Detection of Nucleobases

Gemma Davison, Tabitha Jones, Jia Liu, Juhwan Kim, Yidan Yin, Doeun Kim, Weng-I Katherine Chio, Ivan P. Parkin,* Hyeon-Ho Jeong,* and Tung-Chun Lee*

Hybrid plasmonic nanojunctions with optimal surface-enhanced Raman scattering (SERS) activity are designed via a computer-aided approach, and fabricated via time-controlled aqueous self-assembly of core@shell gold@silver nanoparticles (Au@Ag NPs) with cucurbit[7]uril (CB7) upon simple mixing. The authors showed that SERS signals can be significantly boosted by the incorporation of a strong plasmonic metal and the spectral alignment between the maximal localized surface plasmon resonance (LSPR) and a laser wavelength used for SERS excitation. In a proof-of-concept application, SERS detection of nucleobases with a 633-nm laser has been demonstrated by positioning them within the nanojunctions via formation of host–guest complexes with CB7, achieving rapid response with a detection limit down to sub-nanomolar concentration and an enhancement factor (EF) up to $\approx 10^9$ – 10^{10} , i.e., the minimum required EF for single-molecule detection. Furthermore, machine-learning-driven multiplexing of nucleobases is demonstrated, which shows promise in point-of-care diagnosis of diseases related to oxidative damage of DNA and wastewater-based epidemiology.

fingerprints in the form of Raman scattering signals are significantly enhanced when target molecules are in close proximity to the surface of plasmonic nanostructures.^[1] In particular, SERS detection schemes show promise in point-of-care biosensing and on-site environmental monitoring owing to their key advantages, including high sensitivity, multiplexing capability, minimal sample preparation, water tolerance, and compatibility to portable devices. Nevertheless, their widespread utilization is still hindered by the challenge in developing a facile fabrication scheme for highly precise and reproducible SERS substrates.

Self-assembly of plasmonic nanoparticles (NPs) and other related techniques emerge as scalable approaches for preparing SERS substrates. In order to obtain reproducible SERS signals, sig-

1. Introduction

Surface-enhanced Raman scattering (SERS) spectroscopy finds applications in trace chemical detection where molecular


nificant progress has been made on developing synthetic routes toward dimers and oligomers of NPs with a precise interparticle spacing. In addition to SERS, plasmonic nanojunctions are also important in photovoltaics and fluorescence-based detection analysis. Consequently, a plethora of different assembly approaches have been investigated.^[2] For instance, DNA-mediated plasmonic nanojunctions, including core–shell NPs,^[3] dimers,^[4] nanorod chains,^[5] and even chiral nanostructures,^[6] have been realized but their minimum gap size is larger than 1 nm due to essential pairs of DNA strands for assembly, ultimately reducing the enhancement factor in SERS signal. Meanwhile, their mass-production remains a challenge for industrial applications. The formation of multijunctions via aggregation of colloidal NPs by breaking the charge balance between NPs is another route for mass-production of SERS substrates, but uniform nanojunctions, i.e., reliable SERS intensity throughout the whole sample, have been difficult to achieve.

Notably, aqueous self-assembly of Au NPs mediated by cucurbit[*n*]urils (CB_{*n*}, *n* = 5–8), which are a family of macrocyclic host molecules, remains arguably one of the most facile means of forming plasmonic junctions with a precise sub-nanometer gap, as it can be achieved by simply mixing commercially available components.^[7,8] Moreover, one unique feature of the CB–Au NP system is that target molecules can be selectively captured by CBs that subsequently position them at

G. Davison, T. Jones, J. Liu, Y. Yin, W.-I. K. Chio, T.-C. Lee
Institute for Materials Discovery
University College London
WC1H 0AJ, London, UK
E-mail: tungchun.lee@ucl.ac.uk

G. Davison, T. Jones, J. Liu, Y. Yin, I. P. Parkin, T.-C. Lee
Department of Chemistry
University College London
WC1H 0AJ, London, UK
E-mail: i.p.parkin@ucl.ac.uk

J. Kim, D. Kim, H.-H. Jeong
School of Electrical Engineering and Computer Science
Gwangju Institute of Science and Technology
Cheomdangwagi-ro 123, 61005 Gwangju, Republic of Korea
E-mail: jeong323@gist.ac.kr

 The ORCID identification number(s) for the author(s) of this article can be found under <https://doi.org/10.1002/admt.202201400>.

© 2023 The Authors. Advanced Materials Technologies published by Wiley-VCH GmbH. This is an open access article under the terms of the Creative Commons Attribution License, which permits use, distribution and reproduction in any medium, provided the original work is properly cited.

DOI: 10.1002/admt.202201400

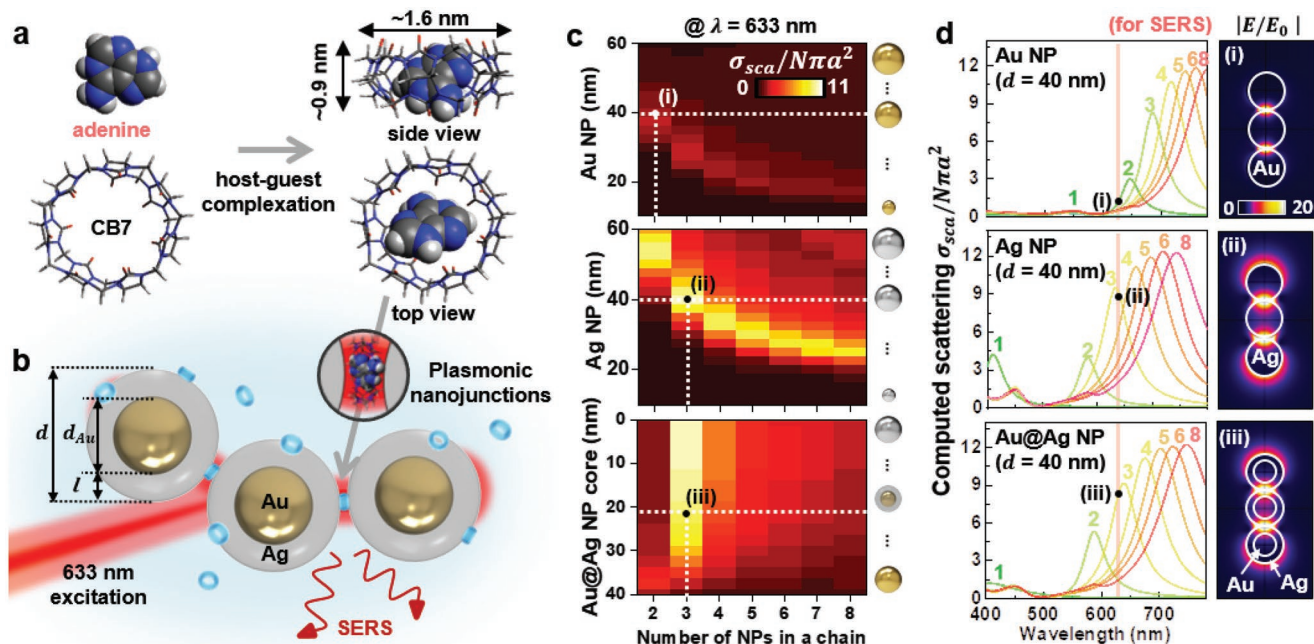


Figure 1. Hybrid plasmonic nanojunctions for sensing of nucleobases. a) Formation of a host–guest complex between a nucleobase and CB7. b) Self-assembled hybrid nanojunctions, made of Au@Ag core–shell nanoparticles and the CB complexes. c) Surface-area normalized scattering cross-sections of the hybrid plasmonic nanojunctions at 633 nm as functions of their diameter (or diameter of the core for Au@Ag NP) and number in a linear chain; top: Au NP, middle: Ag NP, bottom: Au@Ag NP. The strongest conditions for each are marked with roman numerals (i–iii). d) Their normalized scattering spectra and associated optical field enhancements.

the center of a plasmonic hotspot within the nanoaggregates, resulting in intense SERS signals.^[9] Previous work on CB–Au NPs has demonstrated quantitative detection of neurotransmitters,^[10] explosive markers,^[11] and biomarkers in urine.^[12,13] Nevertheless, precedent examples mainly relied on commercial Au NPs ($d = 40\text{--}60\text{ nm}$) that exhibit poor spectral alignment between the localized surface plasmon resonance and the SERS excitation laser when aggregation progresses.

Herein, we showed that a significant increase in SERS signal (>fivefold w.r.t. CB–Au NPs formed by 40-nm Au NPs) can be achieved via the incorporation of a strong plasmonic metal and the spectral alignment between the localized surface plasmon resonance (LSPR) and the 633-nm excitation laser using a computer-aided design approach. Core–shell NPs consisting of a 20-nm Au core and a Ag shell of variable thickness were chosen as our model system due to ease of synthesis and their tunable spectral properties.^[14–16] The optimal thickness of the Ag shell was predicted by computing the normalized scattering cross-section at 633 nm using numerical simulation for various degrees of aggregation, approximated by a linear chain of Au NPs with 0.9-nm interparticle spacing (Figure 1). CB7–Au@Ag NP hybrid plasmonic nanojunctions were then prepared and investigated experimentally. In a proof-of-concept application, SERS detection of nucleobases, which are biomarkers for diseases related to oxidative damage of DNA^[17–19] and bacterial infection,^[20–22] has been demonstrated by positioning them at the nanojunctions via novel host–guest complexation with CB7. Our scheme exhibits rapid response and a detection limit down to 10^{-10} M in the case of spectrally aligned CB7–Au@Ag NPs, which show an enhancement factor (EF) up

to $\approx 10^9\text{--}10^{10}$, achieving the minimum required EF for single-molecule detection.^[3,23] Furthermore, multiplexing of nucleobases in binary mixtures was realized with high accuracy using an artificial neural network model.

2. Results and Discussion

2.1. Computer-Aided Design of Hybrid Plasmonic Nanojunctions

Cucurbit[n]urils are effective mediators for controlled aggregation of colloidal metallic nanoparticles to form accessible plasmonic nanojunctions of <1-nm gap distance, since they are rigid and can strongly bind to metal surfaces (Figure 1a,b). Furthermore, the host–guest chemistry of CBs allows capturing of single (or few) molecules within the plasmonic nanojunctions, enabling highly sensitive (even single-molecular level) SERS measurement.^[24] Here, we used CB7s as a host to tightly trap single nucleobases in the cavity (Figure 1a), generating well-defined plasmonic junctions for theoretical modeling and experimental data analysis (Figure 1b). According to CB7's geometrical dimension and optical properties,^[9] for simplicity in simulation, the gap distance between NPs in the aggregate was fixed at 0.9 nm with constant refractive indices, $n = 1.33$ and $k = 0$, through the whole visible regime. The plasmonic scattering and optical field enhancement were numerically calculated at 633 nm wavelength, since SERS at 633 nm permits flexibility in spectral engineering of the LSPR band while only requiring simple optical rig working in the visible range

(Figure 1c,d). Note that only bright plasmon modes were considered in this work, while further improvement can potentially be achieved via simultaneously optimizing the dark modes that are known to also to play a crucial role in the generation of maximized local fields for spectroscopic performance.^[25]

Three types of plasmonic nanoparticles, Au NP, Ag NP, and Au@Ag NP were modeled with different sizes (10–60 nm), and numbers in a linear chain (2–8) (Figure 1c and Figure S1, Supporting Information). In the case of Au NPs in the top panel of Figure 1c, the dimer of ≈ 40 -nm Au NPs shows the strongest plasmonic scattering at 633 nm. However, in practice the concentration of dimer in the experiment decreases shortly after the aggregation begins,^[9] rapidly red-shifting the LSPR peak into NIR (top panel in Figure 1d). It is thus practically not preferable. In contrast, Ag NPs inherently show stronger and blue-shifted plasmonic scattering than those found in the same geometrical dimensions of Au NPs, as shown in the middle panel in Figure 1c. The trimer of ≈ 40 -nm Ag NPs gives rise to the strongest scattering of Ag NPs at 633 nm, which is five times stronger than those supported by Au dimers. Moreover, trimers can be formed readily at the early stage of the aggregation and their spectral contribution can be sustained (see below for experimental details). However, it is challenging to synthesize Ag NPs with a predefined diameter and a narrow size distribution in the absence of any strongly binding ligands or surfactants, which will hinder the subsequent formation of plasmonic nanojunctions and introduce undesired background Raman signals.^[26]

We thus exploited the advantages of each type of NPs by formulating their core@shell NPs. The synthesis of Au NPs is relatively easy with precise and accurate control over their size, while growing Ag on Au NPs only involves the use of citrate ions as the reducing agent and the ligand,^[27] so we selected the Au NP as a core and coated it with a continuous shell of Ag, i.e., Au@Ag NPs. The scattering cross-sections of 40-nm Au@Ag NPs at 633 nm were then calculated for changes in both sizes of their core and shell parts as well as the number of NPs in a chain while keeping their overall diameter unchanged ($= 40$ nm), as shown in the bottom panel of Figure 1c. Interestingly, when the Ag shell thickness is thicker than ≈ 8 nm, the Au@Ag NPs behave as Ag NPs of the same overall size, and almost reach the strongest scattering of Ag trimers at 633 nm, as expected. Informed by the modeling predictions, we aimed to synthesize Au@Ag trimers whose core Au NP is smaller than 24 nm and coat the Ag shell layer to reach the overall diameter up to 40 nm, which will then be aggregated in the form of trimers (or spectrally similar nanostructures, see Figure S2, Supporting Information, for details) with <1 -nm spaced plasmonic nanojunctions to achieve maximal SERS enhancement.

2.2. Facile Synthesis of Hybrid Plasmonic Nanojunctions

Fabrication of plasmonic junctions consists of three bottom-up steps, **Figure 2**: (i) synthesis of colloidal Au NPs, (ii) Ag shell coating around colloidal Au NPs in solution, and (iii) their self-assembly mediated by CB molecules (see Experimental Section for details). First, the colloidal solution of 22-nm Au NPs was chemically synthesized as a core part of Au@Ag NPs. This size

is deliberately chosen as it not only offers the colloidal Au NPs with their narrow size distribution but also allows room for controlling the thickness of the Ag shell layer to optimize the SERS enhancement, eventually satisfying requirements from the above simulation. Then, a continuous Ag shell layer was subsequently formed around Au NPs using solution chemistry, readily allowing us to tune their thickness with ≈ 1 nm precision via repeating the coating process, Figure 2a. The colors of the associated colloidal Au@Ag NPs changed from pink to orange, and their structural dimensions were measured by transmission electron microscopy (TEM), as shown in the bottom panel in Figure 2a. The core-shell morphology was also confirmed using Scanning Transmission Electron Microscopy (STEM) – Energy Dispersive X-ray spectroscopy (EDS) elemental mapping (Figure S3, Supporting Information). Since the atomic number of Au is significantly larger than that of Ag, the darker region of the Au@Ag NPs in the bright-field TEM images indicates the Au core and the translucent region represents the Ag shell layer. Average overall size (d) of the NPs was calculated by plotting the size distributions of 150 NPs measured by TEM for each growth step, Figure 2b. The Ag shell thickness (l) can then be calculated by $0.5 \times (d - d_{\text{Au}})$, giving l ranging from 1.5 to 17.5 nm for $d_{\text{Au}} = 22$ nm. These values agree with the results from optical extinction spectroscopy, dynamic light scattering and the numerical modeling, i.e., LSPR signals resulting from the dimension and intrinsic nature of plasmonic materials of Au@Ag NPs, Figure 2c and Figure S4 (Supporting Information). The peak wavelengths of the LSPR features gradually blue-shift from 526 to 410 nm as the thickness of the Ag shell layer increases, useful for the subsequent spectral alignment for SERS experiment below.

Finally, precise plasmonic nanojunctions with <1 nm gaps can be formed upon addition of CB7 molecules that mediate controlled aggregation of colloidal Au@Ag NPs (here, 9 nm Ag shell thickness), Figure 2d. Evidence for the aggregation of NPs was provided through the color change of the solution from orange to brown upon the addition of CB7, and the appearance of nanoaggregates in the TEM images. We also tracked the aggregation kinetics via time-lapse dynamic light scattering (DLS) measurements and extinction spectroscopy, Figure 2e–g. The DLS data in the top panel of Figure 2e show the gradual increase in the total hydrodynamic size of the aggregates, matching to the increase in the effective chain length of the NPs from single to dimers (two NPs), trimers (three NPs), and so on. After an initial 30 min, the associated size distributions largely fluctuated (the bottom panel of Figure 2e), due to the randomly formed polydisperse, anisotropic aggregates (see also Figure S5 (Supporting Information) for the change in the averaged hydrodynamic size). The extinction spectra also provide additional evidence with the change in the LSPR features over a period of 2 h, collected every 5 min. The dimers (two NPs) formed with 0.9 nm gap give rise to ≈ 587 nm of the LSPR peak, which gradually red-shifts as the chain length increases to trimers (three NPs) and tetramers (four NPs). After ≈ 30 min, the LSPR intensity began to decay with significant signal broadening, which is the optical feature of the randomly aggregated plasmonic NPs. Optical extinction effects caused by the NP aggregation can be isolated by subtracting proportionated contribution of the unaggregated Au@Ag NPs (Figure 2f).

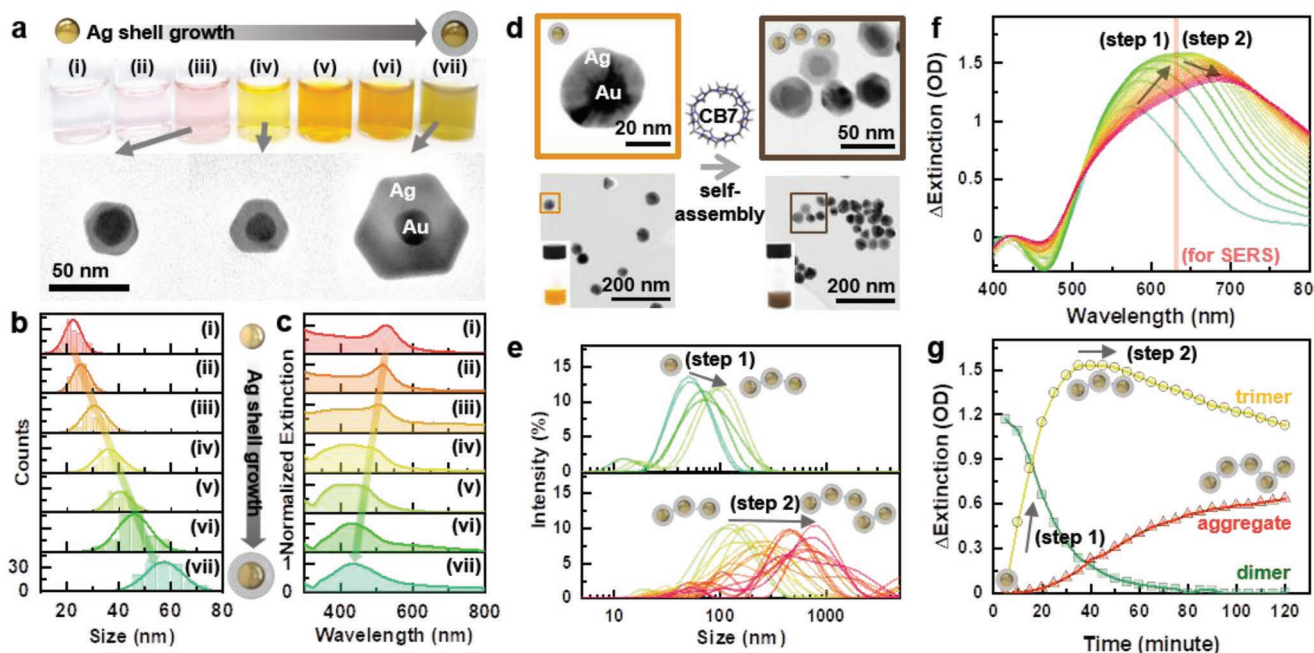


Figure 2. Synthesis of hybrid plasmonic nanojunctions. a) Photographs of synthesized colloidal solutions of Au@Ag nanoparticles with different Ag shell thicknesses, the corresponding bright-field TEM images of selected samples (bottom panel), and b) their sizes measured by TEM, and c) their LSPR spectra. d) TEM images and photographs of sample solutions showing the aggregation of Au@Ag NPs upon addition of CB7. Time-lapse measurements of self-assembly of hybrid plasmonic nanojunctions with CB7 via: e) DLS and f) LSPR spectra after subtraction of the proportionated LSPR contribution from single Au@Ag NPs. g) The deconvoluted LSPR intensities of the dimers, trimers, and aggregates over time by using three Lorentzian fitting at each associated peak wavelength.

Deconvolution of the resultant extinction signal was performed by fitting three Lorentzian functions,^[9] at 587 nm (dimer mode), 638 nm (trimer mode), and 781 nm (aggregate mode), as shown in Figure S6 (Supporting Information). By tracking these three bands over time (Figure 2g), we confirmed that the overall LSPR is initially dominated by the dimer peak at 587 nm, but the second peak attributed to trimer arises over time while the dimer peak rapidly decays. The aggregation of the Au@Ag NPs follows diffusion-limited growth, where higher CB7 concentration results in an increase in probability of NPs sticking together upon collision.^[9] Crucially, under the same experimental condition, the Au@Ag NP trimers (and other spectrally similar nanostructures), optimal for the spectral alignment found in the numerical simulation, can be dominantly achieved by simply controlling the aggregation time, i.e., ≈30 min.

2.3. Nucleobase Sensing Using SERS of Hybrid Nanojunctions

For SERS application, molecular targets should ideally be positioned within or in close proximity to the plasmonic junctions. This scenario can be readily achieved by exploiting the host-guest chemistry of CB7, which can selectively encapsulate guest molecules with complementary size, shape, and charge, prior to mediating the formation of plasmonic junctions. Here, we demonstrated host-guest complexation of CB7 with five different nucleobases (adenine, cytosine, thymine, uracil, and guanine) for the first time.

To verify the formation of host-guest inclusion complexes between CB7 and nucleobases, ¹H NMR measurements of

nucleobases in absence and presence of one equivalent of CB7 were performed, as shown in Figure 3a (and Figure S7, Supporting Information) for adenine and Figures S8–S11 (Supporting Information) for the others. When CB7 and nucleobase are mixed at 1:1 stoichiometry, characteristic upfield shifts of the proton signals caused by the shielding effect of CB7 were observed for all nucleobases, indicating that their corresponding protons are located deep inside the CB7 cavity. Energy-minimized molecular models of CB7-nucleobase complexes calculated based on density functional theory (DFT) support the host-guest geometries derived by ¹H NMR results, inset of Figure 3a. Note that molecular models of the complexes were constructed by assuming the encapsulation of the unprotonated, most stable tautomers in aqueous media at pH 7. The effects of CB7-encapsulation on the p*K*_a and the tautomerism of nucleobases are subjects for further investigation and beyond the scope of this work.

To investigate the validity of our computer-aided design, we initially performed SERS measurements using adenine, which exhibits the strongest SERS signals among other nucleobases, as shown in Figure 3b. In particular, the main Raman bands of adenine powder are attributed to the ring breathing (724 cm⁻¹), rocking (1251 cm⁻¹), stretching (1251 and 1333 cm⁻¹), and bending (1333 cm⁻¹) modes.^[28] SERS spectra of adenine were obtained by mixing aqueous solutions of CB7 with adenine for host-guest complexation, and subsequently adding the resultant mixture to a colloidal solution of 40-nm (22-nm Au core, 9-nm Ag shell) citrate-capped Au@Ag NPs, with final CB7 concentration of 10 μM in all cases. Gratifying to observe, the main SERS signal at 736 cm⁻¹ is ≈five times stronger than those

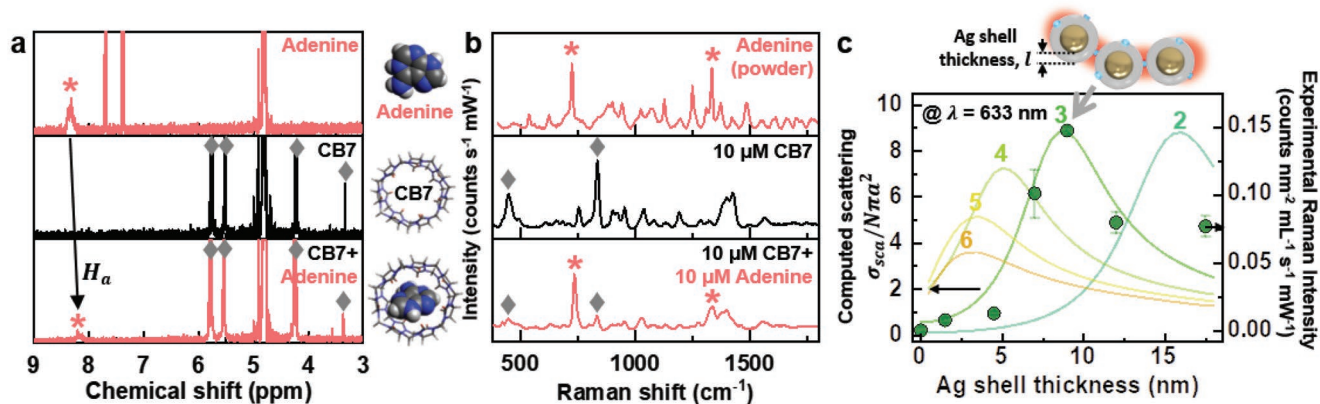


Figure 3. Host-guest complexation of adenine with CB7. a) ^1H NMR spectra (in D_2O) and b) Raman spectrum of adenine powder, and SERS spectra of CB7 and 1:1 CB7-adenine host-guest complex using Au@Ag NPs in ≈ 2 mM aqueous citrate solution from top to bottom. In the middle, corresponding energy-minimized molecular models at CPCM/wB97X-D/6-31G* level of theory. c) SERS intensity of $1\ \mu\text{M}$ adenine at $736\ \text{cm}^{-1}$ using Au@Ag NPs with shell thickness l ranging from 1.5 to 17.5 nm for $d_{\text{Au}} = 22$ nm, overlaid with computed surface-area normalized scattering cross-sections of different effective chain lengths of Au@Ag NPs.

exhibited by the nanoaggregates of CB7 and 40-nm Au NPs (Figure S12, Supporting Information), which perfectly agrees with the numerical prediction in Figure 1c. The stronger SERS intensity allows us to “see” a lower concentration of target molecules, i.e., better sensing performance.

To further verify the effects of the Ag shell thickness, we performed SERS measurements of CB7-adenine complexes using Au@Ag NPs with shell thickness l ranging from 1.5 to 17.5 nm for $d_{\text{Au}} = 22$ nm, and their SERS intensities at $736\ \text{cm}^{-1}$ are plotted in Figure 3c. Our numerical simulation predicts that for trimers the surface-area normalized scattering cross-section at 633 nm reaches a maximum at a shell thickness of ≈ 9 nm, whereas for dimers this value becomes 16 nm. Given that the SERS spectra were measured at around 20–30 min after the addition of CB7 complexes, the majority of the nanoaggregates existed in the form of trimers and other spectrally similar structures (Figure 2g). In this scenario, the experimental SERS intensity per NP surface area increases up to a maximum as the shell thickness increases to 9 nm due to maximal spectral alignment, while decreases when the shell becomes thicker than 9 nm due to a rapidly declining population of dimers. Notably, our experimental observations in SERS closely agree with the predictions of the numerical simulation for the ideal core diameter, shell thickness, and effective NP chain length (as shown in Figure 1). All in all, trimer and spectrally similar nanoaggregates, which are readily formed via time-controlled aqueous self-assembly, can serve as optimal nanostructures for nucleobases sensing when a 633-nm laser is used for SERS enhancement supported by the plasmonic nanojunctions of Au@Ag NPs.

Based on the optimal design, we then demonstrated the fidelity of the Au@Ag hybrid plasmonic nanojunctions for quantitative SERS sensing of all types of nucleobases, Figure 4a. In particular, adenine was dissolved in deionized water and mixed with CB7 at various concentrations, then a SERS titration was performed across a concentration range of 1 nM to 10 μM in the presence of 10 μM CB7 and 40-nm Au@Ag NPs (Figure 4b), where the Raman intensity was plotted against the adenine concentration for the main band at 736

cm^{-1} (Figure 4c). At lower concentrations (1 nM–1 μM), the SERS intensity follows a power law ($R^2 = 0.98$), while the SERS intensity starts to saturate above 1 μM possibly due to the limited number of the CB7 cavities in the plasmonic junctions. The theoretical limit of detection (LoD) for adenine has been calculated by taking into account the signal-to-noise ratio (SNR) of the spectra. The noise was measured from a region of the spectrum with no Raman peaks attributed to adenine, CB7, water or other background molecules (1600–1900 cm^{-1}). The LoD was calculated by dividing the concentration (1 nM) by the corresponding SNR (6), giving a value of 0.17 nM, Figure 4d. The enhancement factor (EF) at 1 μM adenine was estimated to be between $\approx 2.6 \times 10^9$ – 1.3×10^{10} through considering the saturated concentration of plasmonic hotspots and a reasonable range of binding constants of the CB7-adenine complexes (see Section S13, Supporting Information, for a detailed calculation). Note that the achieved EF is considered sufficient for single-molecule detection.

Detection of other nucleobases (cytosine, thymine, uracil, and guanine) was also investigated to explore potential applications in medical diagnosis, Figure 4e,f. The SERS peaks of the nucleobases (Table S1, Supporting Information) are slightly shifted in comparison with those exhibited by their powder form (Figure S14, Supporting Information), which can be commonly attributed to the weak interactions between the nucleobase molecules and the surface of Au@Ag NPs. SERS intensity and concentration of cytosine, guanine, uracil, and thymine are all well fitted with a power law, although the guanine data showed a relatively poor R^2 (0.61–0.72) due to its low solubility in water, Figure 4f. The LoD are 2.6 nM for cytosine, 1.4 nM for thymine, 27 nM for uracil, and 15 nM for guanine (Figure 4d). A comparison of nucleobase detection limits for solution-based SERS systems reported in the literature is included in Section S16 (Supporting Information).

As a proof-of-concept application, to mimic biologically relevant media, nucleobases were dissolved in phosphate-buffered saline (PBS) and mixed with CB7. SERS titrations were subsequently performed for nucleobase concentrations between 0.1 and 5 μM by adding the CB7-nucleobase complexes to

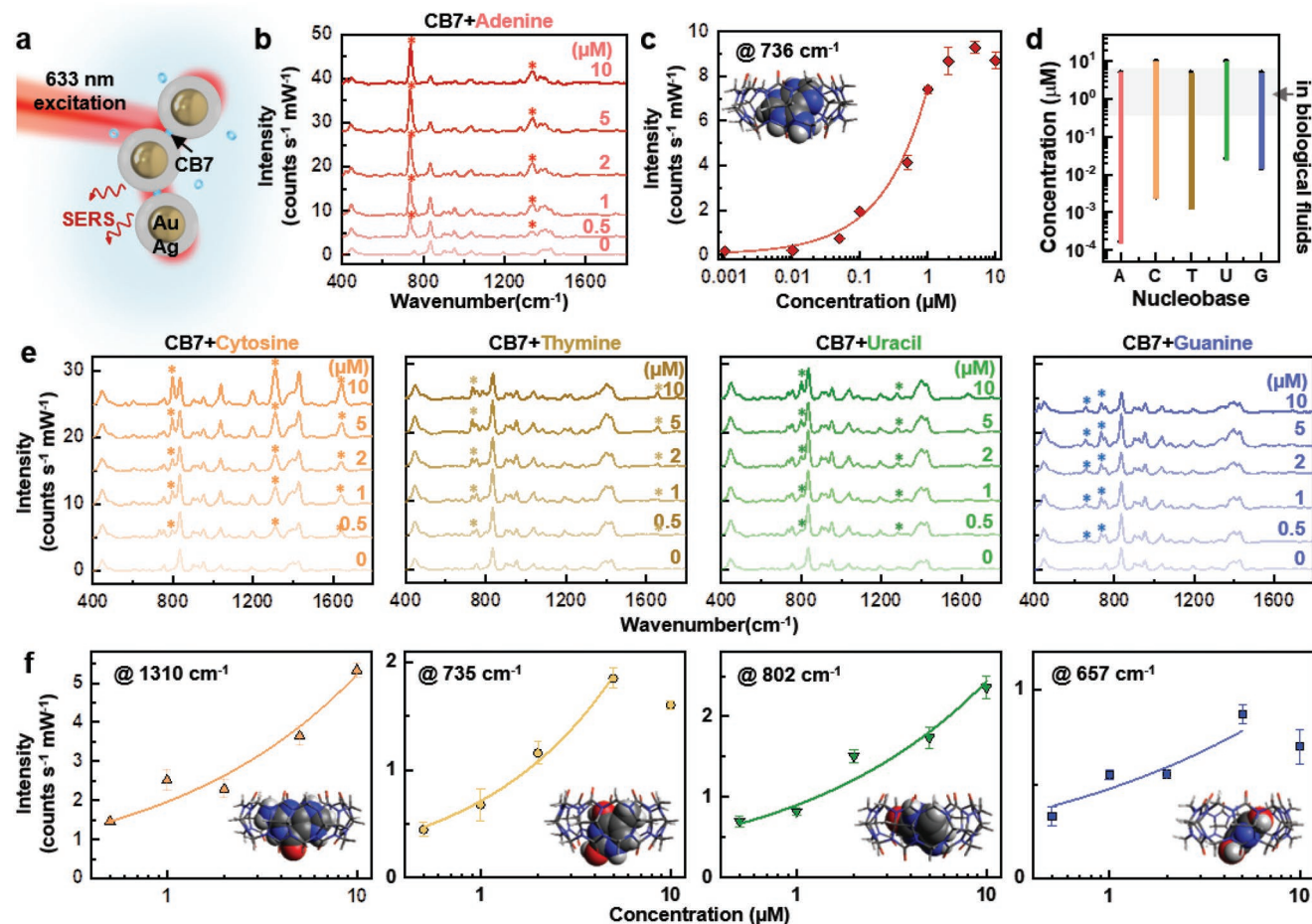


Figure 4. Nucleobase sensing using SERS. a) Detection of nucleobases using hybrid plasmonic nanojunctions. b) SERS titration of adenine using CB7-Au@Ag NPs in ≈ 2 mM aqueous citrate solution and c) associated Raman intensity as a function of concentration of adenine. d) The detection ranges of nucleobases using the hybrid plasmonic junctions extracted from: e) SERS titrations of nucleobases, with; f) plots of Raman intensity against concentration. All SERS spectra presented were measured in ≈ 2 mM aqueous citrate solution.

citrate-capped 40-nm Au@Ag NPs (Figure S14, Supporting Information). The final concentrations of the solutes are given in Table S7 (Supporting Information). The resultant SERS signals remain generally observable (except for thymine) but significantly reduced, probably due to the weakened host-guest binding between CB7 and the nucleobases as a result of competitive binding of Na^+ and K^+ ions from the PBS. Despite the weakened signal, SERS intensity and concentration can be well fitted by power laws for all nucleobases but thymine. Interestingly, guanine exhibited a similar signal intensity but a much better correlation ($R^2 = 0.98$, Figure S14b, Supporting Information) when predissolved in PBS than in water, likely due to its enhanced solubility in PBS.

It is known that the average nucleobase concentration in plasma and extracellular fluids is in the range of 0.4–6 μM .^[29] For instance, the concentrations of adenine liberated from HeLa cells (derived from cervical cancer cells) and from A549 cells (from cancerous lung tissue) are 4.69 and 3.11 μM , respectively.^[30] Thus, our SERS detection scheme based on hybrid plasmonic nanojunctions of CB7-Au@Ag NP covers medically relevant concentrations for all nucleobases. The nanomolar LoD allows SERS measurements to be performed on highly

diluted (e.g., 1000 \times dilution) biological samples that subsequently minimize the associated matrix effects.^[12]

2.4. Machine-Learning-Driven SERS Multiplexing

Multiplexed detection was investigated for mixtures of adenine and cytosine predissolved in water and in PBS. For both water and PBS, 30 different compositions were analyzed with five SERS spectra being recorded for each composition, Figure 5 in PBS and Figure S15 (Supporting Information) in water. The concentration of each nucleobase ranged between 0 and 5 μM , so that the total analyte concentration never exceeded that of CB7 (10 μM), minimizing the undesired effects of competitive binding with CB7 between the two molecular targets. The characteristic Raman peaks of adenine (736 cm^{-1}) and cytosine (1310 cm^{-1}) identified in the single-analyte spectra can be observed in the spectra of binary mixtures, serving as a promising preliminary indication for the viability of quantitative multiplexing.

To fully exploit the information of the entire SERS spectral dataset, machine-learning models were applied to the full

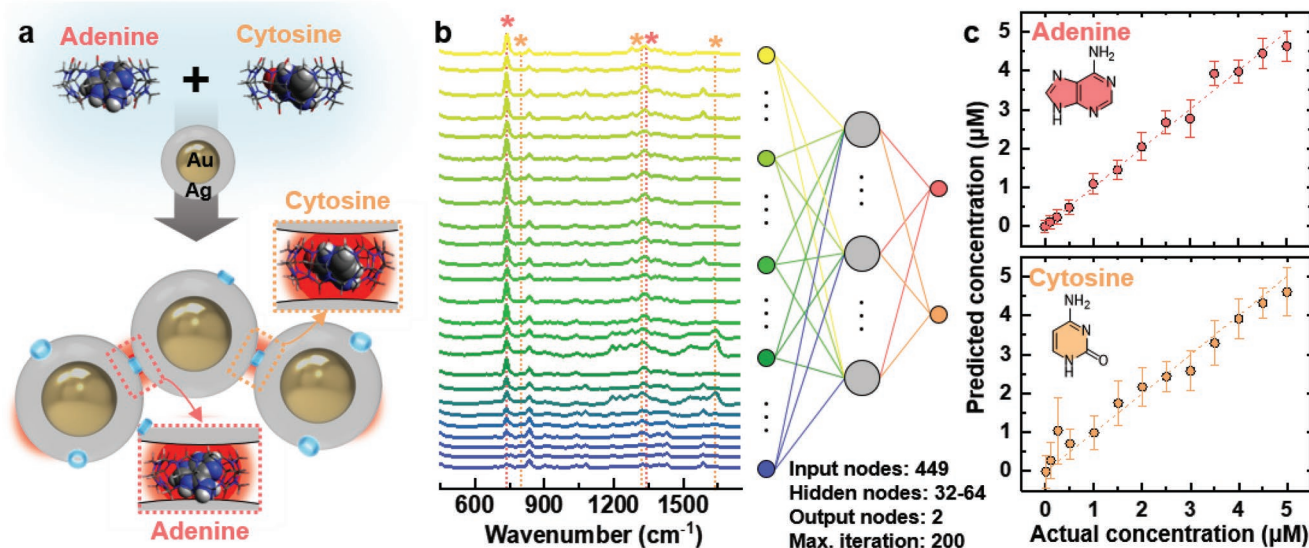


Figure 5. Multiplexing of a mixture containing CB7-adenine and CB7-cytosine complexes using Au@Ag NPs. a) Schematic. b) SERS measurements for solutions consisting of various concentrations of CB7-adenine and CB7-cytosine, where the nucleobase targets were predissolved in PBS media, and c) associated machine-learning-driven data analysis.

spectral range of all spectra.^[31] It is known that subtle spectral features other than the main Raman peaks can contribute significantly to the predictive capability of the model.^[32] Here, we employed multilayer perceptrons (MLPs), one of the most popular types of feed-forward artificial neural network, for quantitative multiplexing of adenine and cytosine.^[33] MLPs consist of three layers of neurons—an input layer, one or more hidden layers, and an output layer. For this work, the MLPs have 449 input nodes (intensities at each wavenumber shift in the SERS spectra after preprocessing) and two output nodes (number of analytes in the study). Details of the optimized MLP architecture are given in Section S19 (Supporting Information). The water and PBS datasets each contained 175 spectra recorded from the 30 different adenine and cytosine mixtures. Prior to any modeling, asymmetric least squares (ALS) baseline correction was applied to the whole spectra and standard normal variate normalization was performed.^[34,35] To prevent overfitting of the MLPs, the models were evaluated using the bootstrapping random resampling procedure.^[36,37] A total of 1000 bootstrapping iterations were performed and the mean R^2 and root-mean-square error of prediction (RMSEP) values are calculated to assess the performance of the models.

The results from the MLPs trained with the PBS dataset are shown in Figure 5c (Figure S15, Supporting Information, for the water dataset). In both cases, the predicted concentrations versus the actual concentrations are very close to the $y = x$ line, indicating excellently fitted models. For the nucleobase targets predissolved in PBS (and in water), the R^2 values for the adenine and cytosine predictions are 0.963 (0.948) and 0.889 (0.908), respectively. The RMSEP values for the PBS (and water) samples are 0.341 μM (0.411 μM) for adenine and 0.599 μM (0.548 μM) for cytosine. The impressive performance of these MLP models demonstrates the power of machine learning to identify subtle patterns in SERS

spectra and use them to make accurate quantitative concentration predictions. In real-world applications, machine-learning models, such as MLPs, can enable fast interpretation of complex, noisy spectra without the need for specialized, trained operators. However, care must be taken with artificial neural networks. They are often described as “black boxes” because it is difficult to determine how a particular model make its predictions.^[38] These algorithms rely on reliable, representative datasets to make accurate predictions and caution must be applied when gathering the dataset to prevent overfitting.

Although only two nucleobases can be simultaneously detected in this proof-of-concept study, these results illustrate that the CB7-Au@Ag NP system has the potential, when combined with machine learning, for the quantitative multiplexed detection of nucleobases and consequently the diagnosis of diseases.

3. Conclusion

To sum up, we have designed spectrally aligned hybrid plasmonic nanojunctions based on CB7-Au@Ag NPs using a computer-aided approach, where optimal thickness of the Ag shell was predicted for a selected SERS excitation (i.e., 633 nm in our case) using the numerical simulation for various degree of aggregation. Core-shell Au@Ag NPs were synthesized by a facile seed-growth technique and then simply mixed with CB7 to form CB7-Au@Ag NP precise nanojunctions via aqueous self-assembly. The desired nanostructures were confirmed by UV-vis, DLS, and TEM; while the aggregation kinetics of the optimal CB7-Au@Ag NP was elucidated by UV-vis and DLS, showing excellent consistency between the two experimental datasets and with the computed UV-vis spectra across various degree of aggregation.

SERS detection of nucleobases via formation of novel CB7 complexes was selected as a proof-of-concept application to illustrate the effectiveness of our design. Notably, spectrally aligned CB7-Au@Ag NPs ($d_{\text{Au}} \approx 22$ nm, $l \approx 9$ nm, $d \approx 40$ nm) exhibit significantly enhanced SERS signals (>fivefold w.r.t. CB7-Au NPs formed by 40-nm Au NPs), which enable a detection limit down to 10^{-10} M in the case of adenine and an enhancement factor up to $\approx 10^9$ – 10^{10} , achieving that required for single-molecule detection.^[3,23] Finally, multiplexing of nucleobases in binary mixtures was realized with high accuracy using an artificial neural network model. These results show promise in point-of-care diagnosis of diseases related to oxidative damage of DNA, such as cancer and AIDS,^[18,19,39] as well as wastewater-based epidemiology.^[40]

Our approach showcases the use of various established computational models in different stages of the workflow to guide and complement the experimental effort, featuring the numerical models for designing the plasmonic nanojunctions, DFT models for predicting and rationalizing the host–guest binding, as well as artificial neural network for multiplexed SERS data analysis. This combined computational and experimental methodology illustrates how design of novel hybrid plasmonic nanosystems can be achieved in a simple and effective manner, which can inspire our vision in future design processes.

4. Experimental Section

Numerical Simulations: Three-dimensional models were simulated using COMSOL multiphysics 5.6 (incorporated wave optics module). Dielectric functions of gold and silver were taken from the literature.^[41,42] To simplify the calculation, the refractive index of medium was kept as constant $n = 1.33$. The absorption, scattering, and extinction spectra were simulated in 5 nm steps in the wavelength range from 400 to 800 nm and wider range for longer chains up to 12 nanoparticles. The computational domain size was defined with perfectly matched layers in order to calculate in finite space and prevent reflection. The incident light propagated along the z-axis with an x-axis polarization, which was the direction of the chain of nanoparticles.

Materials: Gold(III) chloride solution (HAuCl_4), silver nitrate (AgNO_3), and sodium citrate were all purchased from Sigma-Aldrich for the Au@Ag synthesis. Adenine, cytosine, guanine, uracil, and thymine were purchased from Sigma-Aldrich for the Raman measurements. Cucurbit[7]uril (CB7) was synthesized according to the literature.^[43] All chemicals were used as received, and Milli-Q water was used in all experiments.

Gold Seed Synthesis: Au NPs of ≈ 22 nm were synthesized using a seeded growth method, based on the method described by Bastús et al.^[44] A total of 200 mL of 0.25 mM HAuCl_4 was heated in a two-necked round-bottomed flask in an oil bath at 90 °C for 15 min, with continuous stirring at 700 rpm. 1 mL of 500 mM sodium citrate solution was then added to the HAuCl_4 , and the solution was heated at 90 °C for 30 min, stirring at 700 rpm until the solution turned ruby red.

Core–Shell Au@Ag NPs Synthesis: The 22-nm Au seeds were cooled to 70 °C. 1.34 mL of 25 mM silver nitrate and 1.34 mL of 60 mM sodium citrate were injected, and the solution was maintained at 700 rpm, 70 °C for 30 min. This was repeated to increase the thickness of the Ag shell.

Ultraviolet–Visible Spectroscopy: A UV–vis spectrometer (Ocean Optics Flame spectrometer with DH-mini light source) was used to acquire UV–visible spectra of the samples. Milli-Q water was used to store a reference spectrum and a background spectrum. 1 mL of the Au@Ag

NP solution was transferred into a 1-cm optical path length cuvette and placed in the spectrometer. A 10 ms integration time was used, with 300 scans to average, and a boxcar width of 3. The absorbance spectra were collected in a wavelength range of 180–880 nm.

Transmission Electron Microscopy: A 200 kV JEOL 2100 TEM with a Orius SC200 1 camera was used to obtain images of the samples. A pipette was used to transfer a few drops of the nanoparticle solution onto a Holely carbon TEM grid (300-mesh, Cu), this was left to air dry. Gatan digital micrograph software was used to analyze the images obtained.

Dynamic Light Scattering: A Malvern Zetasizer was used to perform dynamic light scattering (DLS) measurements. 0.5 mL of Au@Ag solution was placed in a cuvette, and DLS measurements were taken before and after the addition of CB7.

Nuclear Magnetic Resonance (NMR) Spectroscopy: All ^1H NMR spectra were recorded by a Bruker Avance III 400 MHz spectrometer at room temperature. All samples were prepared at 1 mM. Samples of free adenine, cytosine, uracil, and thymine, and their 1:1 CB7 included complexes were prepared in deuterium oxide (D_2O). Samples of free guanine and its 1:1 CB7-guanine complex were prepared in 1 mM deuterium chloride (DCl). Chemical shifts (in ppm) were referenced to D_2O with $\delta \approx 4.80$ ppm for ^1H .

Molecular Modeling: Molecular models were optimized using force-field calculations by MMFF94 in Chem3D first and were submitted for full optimization by density functional theory (DFT) calculations at wB97XD/6-31G* and CPCM/wB97XD/6-31G* level of theory using Gaussian. According to the reported pK_a values,^[45,46] all these five nucleobases existed as neutral form at pH 7, and according to the tautomerism study,^[45,47] the most stable tautomer of their neutral form was employed in this work for computational simulations.

Raman Spectroscopy: Measurements were performed using our in-house protocol.^[13] In brief, a Raman spectrometer (Ocean Optics QE Pro Raman) was used with a 632.8 nm helium–neon laser, with a laser power of 22.5 mW. Stock solutions of the nucleobases mixed with CB7 in water were prepared. CB7 of final concentration of 10 μM was used to aggregate the Au@Ag NPs. The CB7-nucleobase complexes were added to the Au@Ag NPs, and 1 mL of solution was placed in a cuvette for measurements. Ten scans to average were taken, with a scan time of 7 s. Origin software was used to perform a baseline correction.

Supporting Information

Supporting Information is available from the Wiley Online Library or from the author.

Acknowledgements

This work was funded by the Leverhulme Trust (grant No. RPG-2016-393). G.D. and T.J. would like to thank the EPSRC M3S CDT (grant No. EP/L015862/1) for sponsoring their studentship. T.J. and T.C.L. acknowledge the Camtech Innovations for contribution to T.J.'s studentship. The authors acknowledge the use of the UK Materials and Molecular Modelling Hub, which are partially funded by EPSRC (grant No. EP/P020194/1). This work was also in part supported by the National Research Foundation of Korea (NRF) grant funded by the Korea government (MSIT) (grant Nos. NRF-2021M3H3A1037899 and NRF-2021R1C1C1005060). The authors acknowledge Dr. S. Firth for assistance with STEM-EDS.

Conflict of Interest

The authors declare no conflict of interest.

Data Availability Statement

The data that support the findings of this study are available from the corresponding author upon reasonable request.

Keywords

computed-aided design, host-guest chemistry, nucleobase detection, plasmonic nanojunctions, surface-enhanced Raman scattering

Received: August 26, 2022

Revised: December 1, 2022

Published online:

- [1] S. Schlücker, *Angew. Chem., Int. Ed.* **2014**, *53*, 4756.
- [2] J. Langer, D. Jimenez de Aberasturi, J. Aizpurua, R. A. Alvarez-Puebla, B. Auguie, J. J. Baumberg, G. C. Bazan, S. E. J. Bell, A. Boisen, A. G. Brolo, J. Choo, D. Cialla-May, V. Deckert, L. Fabris, K. Faulds, F. J. Garcia de Abajo, R. Goodacre, D. Graham, A. J. Haes, C. L. Haynes, C. Huck, T. Itoh, M. Käll, J. Kneipp, N. A. Kotov, H. Kuang, E. C. Le Ru, H. K. Lee, J.-F. Li, X. Y. Ling, et al., *ACS Nano* **2019**, *14*, 28.
- [3] D.-K. Lim, K.-S. Jeon, J.-H. Hwang, H. Kim, S. Kwon, Y. D. Suh, J.-M. Nam, *Nat. Nanotechnol.* **2011**, *6*, 452.
- [4] A. P. Alivisatos, K. P. Johnsson, X. Peng, T. E. Wilson, C. J. Loweth, M. P. Bruchez, P. G. Schultz, *Nature* **1996**, *382*, 609.
- [5] W. Ma, H. Kuang, L. Xu, L. Ding, C. Xu, L. Wang, N. A. Kotov, *Nat. Commun.* **2013**, *4*, 2689.
- [6] A. Kuzyk, R. Schreiber, Z. Fan, G. Pardatscher, E.-M. Roller, A. Högele, F. C. Simmel, A. O. Govorov, T. Liedl, *Nature* **2012**, *483*, 311.
- [7] T.-C. Lee, O. A. Scherman, *Chem. Commun.* **2010**, *46*, 2438.
- [8] T.-C. Lee, O. A. Scherman, *Chemistry* **2012**, *18*, 1628.
- [9] R. W. Taylor, T.-C. Lee, O. A. Scherman, R. Esteban, J. Aizpurua, F. M. Huang, J. J. Baumberg, S. Mahajan, *ACS Nano* **2011**, *5*, 3878.
- [10] S. Kasera, L. O. Herrmann, J. del Barrio, J. J. Baumberg, O. A. Scherman, *Sci. Rep.* **2015**, *4*, 6785.
- [11] W.-I. K. Chio, W. J. Peveler, K. I. Assaf, S. Moorthy, W. M. Nau, I. P. Parkin, M. Olivo, T.-C. Lee, *J. Phys. Chem. C* **2019**, *123*, 15769.
- [12] W.-I. K. Chio, S. Moorthy, J. Perumal, D. U. S., I. P. Parkin, M. Olivo, T.-C. Lee, *J. Mater. Chem. C* **2020**, *8*, 7051.
- [13] W.-I. K. Chio, G. Davison, T. Jones, J. Liu, I. P. Parkin, T.-C. Lee, *J. Vis. Exp.* **2020**, *164*, 61682.
- [14] H.-H. Jeong, E. Choi, E. Ellis, T.-C. Lee, *J. Mater. Chem. B* **2019**, *7*, 3480.
- [15] T. Jones, G. Davison, H.-H. Jeong, T.-C. Lee, in *Nanoscience & Nanotechnology Series*, (Eds: E. Ye, Z. Li), Royal Society of Chemistry, Cambridge **2022**, pp. 33–80.
- [16] S. Bhaskar, A. Rai, K. M. Ganesh, R. Reddy, N. Reddy, S. S. Ramamurthy, *Langmuir* **2022**, *38*, 12035.
- [17] Y. Hou, X. Liu, X. Tang, T. Li, Q. Wu, Y. Jiang, J. Yi, G. Zhang, *Talanta* **2017**, *173*, 107.
- [18] J. Cadet, T. Delatour, T. Douki, D. Gasparutto, J.-P. Pouget, J.-L. Ravanat, S. Sauvaigo, *Mutat. Res./Fundam. Mol. Mech. Mutagen.* **1999**, *424*, 9.
- [19] K. B. Beckman, B. N. Ames, *J. Biol. Chem.* **1997**, *272*, 19633.
- [20] W. R. Premasiri, J. C. Lee, A. Sauer-Budge, R. Théberge, C. E. Costello, L. D. Ziegler, *Anal. Bioanal. Chem.* **2016**, *408*, 4631.
- [21] T. P. Lynk, C. S. Sit, C. L. Brosseau, *Anal. Chem.* **2018**, *90*, 12639.
- [22] S. Wen-Yu Chiu, H.-W. Cheng, Z.-X. Chen, H.-H. Wang, M.-Y. Lai, J.-K. Wang, Y.-L. Wang, *Phys. Chem. Chem. Phys.* **2018**, *20*, 8032.
- [23] Y. Wang, J. Irudayaraj, *Philos. Trans. R. Soc. Lond. B Biol. Sci.* **2013**, *368*, 20120026.
- [24] N. H. Kim, W. Hwang, K. Baek, Md. R. Rohman, J. Kim, H. W. Kim, J. Mun, S. Y. Lee, G. Yun, J. Murray, J. W. Ha, J. Rho, M. Moskovits, K. Kim, *J. Am. Chem. Soc.* **2018**, *140*, 4705.
- [25] K. Kneipp, H. Kneipp, J. Kneipp, *Chem. Sci.* **2015**, *6*, 2721.
- [26] D. D. Evanoff, G. Chumanov, *J. Phys. Chem. B* **2004**, *108*, 13948.
- [27] R. G. Freeman, M. B. Hommer, K. C. Grabar, M. A. Jackson, M. J. Natan, *J. Phys. Chem.* **1996**, *100*, 718.
- [28] F. Madzharova, Z. Heiner, M. Gühlke, J. Kneipp, *J. Phys. Chem. C* **2016**, *120*, 15415.
- [29] T. W. Traut, *Mol. Cell. Biochem.* **1994**, *140*, 1.
- [30] M. Y. Emran, S. A. El-Safty, M. M. Selim, A. Reda, H. Morita, M. A. Shenashen, *Carbon* **2021**, *173*, 1093.
- [31] W.-I. K. Chio, J. Liu, T. Jones, J. Perumal, U. S. Dinis, I. P. Parkin, M. Olivo, T.-C. Lee, *J. Mater. Chem. C* **2021**, *9*, 12624.
- [32] S. Guo, J. Popp, T. Bocklitz, *Nat. Protoc.* **2021**, *16*, 5426.
- [33] C. M. Bishop, *Neural Networks for Pattern Recognition*, Clarendon Press, Oxford **1995**.
- [34] P. H. C. Eilers, *Anal. Chem.* **2003**, *75*, 3631.
- [35] O. Alharbi, Y. Xu, R. Goodacre, *Anal. Bioanal. Chem.* **2015**, *407*, 8253.
- [36] O. Alharbi, Y. Xu, R. Goodacre, *Analyst* **2014**, *139*, 4820.
- [37] B. Efron, R. J. Tibshirani, *An Introduction to the Bootstrap*, CRC Press, New York, NY **1994**.
- [38] Z. Zhang, M. W. Beck, D. A. Winkler, B. Huang, W. Sibanda, H. Goyal, *Ann. Transl. Med.* **2018**, *6*, 216.
- [39] M. D. Greenberg, *Radical and Radical Ion Reactivity in Nucleic Acid Chemistry*, John Wiley & Sons, Hoboken, NY **2009**.
- [40] W.-I. K. Chio, H. Xie, Y. Zhang, Y. Lan, T.-C. Lee, *Trends Analyt. Chem.* **2022**, *146*, 116485.
- [41] P. B. Johnson, R. W. Christy, *Phys. Rev. B* **1972**, *6*, 4370.
- [42] E. D. Palik, *Handbook of Optical Constants of Solids*, Academic Press, Cambridge, MA **1998**.
- [43] J. Lagona, P. Mukhopadhyay, S. Chakrabarti, L. Isaacs, *Angew. Chem., Int. Ed.* **2005**, *44*, 4844.
- [44] N. G. Bastús, J. Comenge, V. Puntès, *Langmuir* **2011**, *27*, 11098.
- [45] V. Verdolino, R. Cammi, B. H. Munk, H. B. Schlegel, *J. Phys. Chem. B* **2008**, *112*, 16860.
- [46] S. Ganguly, K. K. Kundu, *Can. J. Chem.* **1994**, *72*, 1120.
- [47] M. T. Nguyen, A. K. Chandra, T. Zeegers-Huyskens, *J. Chem. Soc., Faraday Trans.* **1998**, *94*, 1277.